
Ultrahigh Energy Storage in Tungsten Bronze Dielectric Ceramics through a Weakly Coupled Relaxor Design

Yangfei Gao ^{a #}, Wenjing Qiao ^{a #}, Xiaojie Lou ^{a *}, Zizheng Song ^b, Xiaopei Zhu ^c, Liqiang He ^a, Bian Yang ^{c *}, Yanhua Hu ^d, Jinyou Shao ^{a, e}, Danyang Wang ^f, Zibin Chen ^{b *} and Shujun Zhang ^{g *}

^a *Frontier Institute of Science and Technology, State Key Laboratory for Mechanical Behavior of Materials, and Xian Key Laboratory of Electric Devices and Materials Chemistry, Xi'an Jiaotong University, Xi'an 710049, China*

^b *Department of Industrial and Systems Engineering, The Hong Kong Polytechnic University, Hong Kong, China*

^c *School of Materials Science and Engineering, Xi'an University of Technology, Xi'an, Shaanxi 710048, China*

^d *Department of Chemical Engineering, Ordos Institute of Technology, Ordos 017000, P. R. China*

^e *Micro-and Nano-Technology Research Center, State Key Laboratory for Manufacturing Systems Engineering, Xi'an Jiaotong University, Xi'an, Shaanxi, 710049, P. R. China*

^f *School of Materials Science and Engineering, UNSW, Sydney, NSW 2052, Australia*

^g *Institute for Superconducting and Electronic Materials, AIIM, University of Wollongong, Wollongong, NSW, Australia*

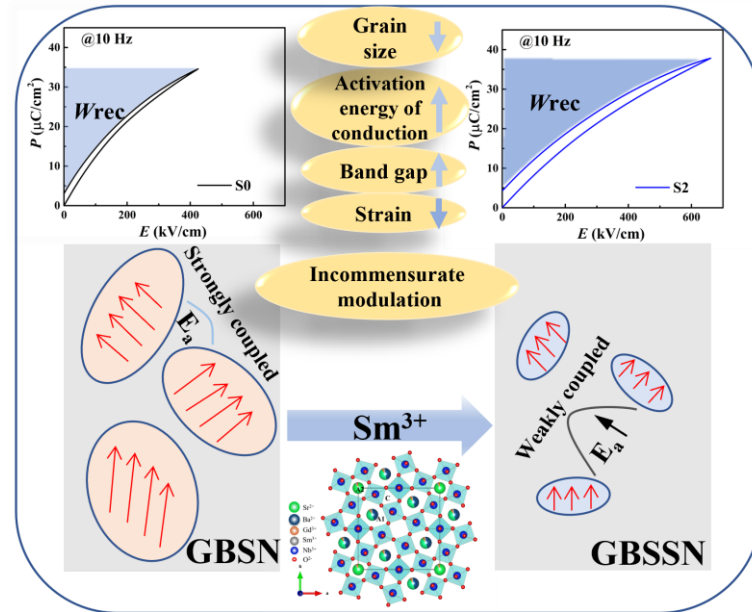
#These authors contribute equally to this work.

*Corresponding author's email address: *xlou03@mail.xjtu.edu.cn* (X.J. Lou),
yangbian@xaut.edu.cn (B. Yang), *zi-bin.chen@polyu.edu.hk* (Z.B. Chen),
shujun@uow.edu.au (S.J. Zhang)

Abstract:

Dielectric energy-storage capacitors, known for their ultra-fast discharge time and high-power density, find widespread applications in high-power pulse devices. However, ceramics featuring a tetragonal tungsten bronze structure (TTBs) have received limited attention due to their lower energy-storage capacity compared to perovskite counterparts. Herein, we report a TTBs relaxor ferroelectric ceramic based on the $\text{Gd}_{0.03}\text{Ba}_{0.47}\text{Sr}_{0.485-1.5x}\text{Sm}_x\text{Nb}_2\text{O}_6$ composition, exhibiting an ultrahigh recoverable energy density of 9 J/cm^3 and an efficiency of 84% under an electric field of 660 kV/cm. Notably, the energy storage performance of this ceramic shows remarkable stability against frequency, temperature, and cycling electric field. The introduction of Sm^{3+} doping was found to create weakly coupled polar nanoregions (PNRs) in the $\text{Gd}_{0.03}\text{Ba}_{0.47}\text{Sr}_{0.485}\text{Nb}_2\text{O}_6$ ceramic. Structural characterizations reveal that the incommensurability parameter increases with higher Sm^{3+} content, indicative of a highly disordered A-site structure. Simultaneously, the breakdown strength is also enhanced by raising the conduction activation energy, widening the band gap, and reducing the electric field-induced strain. This work presents a significant improvement on the energy storage capabilities of TTBs-based capacitors, expanding the material choice for high-power pulse device applications.

Graphical abstract



Keywords: Energy storage; Tetragonal tungsten bronze structure; Dielectrics capacitors; Relaxor ferroelectrics

1. Introduction

In recent years, there has been significant research attention directed towards dielectric capacitors, driven by their ability to fulfill the requirements of energy storage materials with ultrafast discharge rate and high-power density, which is critical for pulsed electronic devices [1-3]. However, the majority of current research has been concentrated on dielectric ceramics with perovskite structures [4-5]. In contrast, tetragonal tungsten bronze (TTB)-structure ferroelectric ceramics, the second-largest category of ferroelectrics, have received comparatively less attention due to their intricate crystal structure and subpar energy storage performance [6-7].

The total energy storage density (W_{total}) of a dielectric capacitor depends on the opposite electrostatic charges separated between two electrodes [8]. W_{rec} , the

recoverable energy density, can be calculated by integrating the area between P_r and P_{\max} on the polarization-electric field hysteresis loop (P - E loop), and the efficiency, η , is given by the ratio of W_{rec} to W_{total} . These are expressed as follows:

$$W_{\text{total}} = \int_0^{P_{\max}} E dP \quad (1)$$

$$W_{\text{rec}} = \int_{P_r}^{P_{\max}} E dP \quad (2)$$

$$\eta = \frac{W_{\text{rec}}}{W_{\text{total}}} \times 100\% \quad (3)$$

where P_r , P_{\max} , and E are the remnant polarization, maximum polarization and electric field, respectively. To attain a high recoverable energy density and efficiency, a large P_{\max} , low P_r , and a high breakdown field (E_b) are required [9]. Relaxor ferroelectrics are particularly advantageous in terms of energy storage performance, amongst the various dielectric materials, including linear dielectrics and nonlinear ferroelectrics [10].

TTBs are a derivative of the perovskite structure, but provides greater flexibility in tailoring the local stoichiometry and lattice structures. The unit cell of TTBs materials can be expressed as $(A1)_4(A2)_2(C)_4(B1)_2(B2)_8O_{30}$, where BO_6 octahedrons combine to form a pentagon A1, a quadrilateral A2, and a triangle C interval. The TTBs materials are categorized into three groups based on the extent to which the ions occupy lattice sites: fully filled (A1, A2, and C intervals are completely occupied by cations), filled (A1 and A2 sites fully occupied, and C sites partially occupied), and unfilled (A1 and A2 intervals partially occupied, while C interval remains empty). The adjustable A1, A2, B1, and B2 sites within TTBs ceramics offer a range of possibilities for tuning

the ion composition, encompassing distinct charges and radii. This, in turn, gives rise to distinct dielectric and ferroelectric properties ^[11].

The disordered occupation of cations across the A-site, B-site, or a combination of both is the primary driving force for the relaxation behavior in TTBs ceramics ^[12]. Cao *et al.*^[13] conducted a study on the relaxation behavior of Gd-doped fully or unfilled Sr₂NaNb₅O₁₅-based TTBs ceramics and achieved a W_{rec} of 2.37 J/cm³ with a high efficiency of 94% by controlling the vacancy and relaxation characteristics within the material. Xu *et al.*^[6] demonstrated that the introduction of Sb⁵⁺ into the B-site of Sr₂Ag_{0.2}Na_{0.8}Nb₅O₁₅-filled TTBs TTBs ceramics resulted in a transition of the crystal structure from an orthorhombic Im2a phase to a tetragonal paraelectric P4/mbm phase, leading to an evolution from typical ferroelectric to relaxor concomitantly. In the resulting P4/mbm phase with a composition of Sr₂Na_{0.8}Ag_{0.2}Nb_{4.7}Sb_{0.3}O₁₅, characterized by reduced unit cell volume, a W_{rec} of 2.27 J/cm³ and an efficiency of 93% were achieved. Peng *et al.* ^[14] employed a multiscale tuning strategy to improve the energy storage performance of TTBs ceramics at various length scales, including the grain, domain, and macroscopic levels. By triggering the dynamic polar nanodomains with enhanced relaxation behavior, the remanent polarization is decreased. Additionally, by refining the grains and increasing the bandgap, a higher breakdown strength was obtained. Consequently, an unfilled Sr_{0.425}La_{0.1}□_{0.05}Ba_{0.425}Nb_{1.4}Ta_{0.6}O₆ TTBs ceramic exhibited a W_{rec} of 5.9 J/cm³ and an efficiency of 85%. In another approach. Yang *et al.*^[15] developed Gd(A-site)/Ta(B-site) co-doped Sr_{0.53}Ba_{0.47}Nb₂O₆-based ferroelectric ceramics, in which the relaxation properties of the matrix was

improved by introducing a commensurate-incommensurate structure modulation. The resultant W_{rec} is 6.23 J/cm^3 at room temperature and over 5 J/cm^3 at $140 \text{ }^\circ\text{C}$. Despite these significant advancements, it's worth noting that TTBS ceramics still lag behind perovskite materials in terms of energy storage performance ^[16].

In this work, we designed and fabricated lead-free tungsten bronze $\text{Gd}_{0.03}\text{Ba}_{0.47}\text{Sr}_{0.485-1.5x}\text{Sm}_x\text{Nb}_2\text{O}_6$ (GBSSN) compounds ($x=0, 0.01, 0.02, \text{ and } 0.03$, abbreviated as S0, S1, S2, and S3, respectively) for energy storage capacitors. Compared to the pristine $\text{Gd}_{0.03}\text{Ba}_{0.47}\text{Sr}_{0.485}\text{Nb}_2\text{O}_6$ (GBSN) ceramic, the introduction of Sm^{3+} enables the tuning of relaxation characteristics and promotes the formation of weakly coupled polar nanoregions (PNRs). As a result, an ultrahigh W_{rec} of 9 J/cm^3 and a remarkable η of 84% were achieved in the $\text{Gd}_{0.03}\text{Ba}_{0.47}\text{Sr}_{0.455}\text{Sm}_{0.02}\text{Nb}_2\text{O}_6$ ceramic under 660 kV/cm , surpassing the previously reported values for TTBS compounds, highlighting the effectiveness of our approach.

2. Results and Discussion

Figure 1(a) shows the unipolar polarization hysteresis loops of S0-S3 prior to their respective breakdown electric fields, which were used to calculate the energy storage performance (Fig. 1(b)). It is evident that the W_{rec} exhibits progression from 5.3 J/cm^3 (S0) to 9 J/cm^3 (S2), and then declines to 6.1 J/cm^3 for S3 due to its reduced E_b . A comparison of the energy storage performance between the studied compositions and other representative lead-free ceramics is showcased in Fig. 1(c). It should be stressed that the energy storage performance of the S2 sample is highly comparable to that of perovskite-structured dielectric ceramics documented in the literature^[17-30]. In Fig. 1(d),

a comparison is made between the energy-storage performance of sample S2 with other TTBs ceramics. It is evident that sample S2, developed in the scope of this study, has the highest recoverable energy density W_{rec} among all TTBs ceramics [6-7, 13-15, 31-41], reaching to a remarkable 9 J/cm³.

To gain a better understanding of how energy storage performance changes with the alteration of Sm³⁺ doping level, Figs. S1(a) and (b) display the hysteresis loops and corresponding energy storage performance under a constant electric field of 350 kV/cm. As the Sm³⁺ content increases, the P - E loops become slimmer, demonstrating a strengthened relaxation behavior. The extracted P_{max} and P_{r} values are given in Fig. S1(c), both of which decrease with the increase in Sm³⁺ content. The corresponding $(P_{\text{max}} - P_{\text{r}})$ values also decrease significantly, leading to a decrease in W_{rec} and an increase in η as the Sm³⁺ doping level increases. As the electric field increases, P_{max} of sample S2 gradually increases, along with a smooth transition current, as shown in Figs. S1(d) and (e). This behavior is indicative of a clear dielectric relaxation for sample S2. Figure S1(f) shows the energy storage performance of sample S2 under different electric fields. It can be seen that with the increase of the electric field, energy storage density gradually increases and efficiency gradually decreases.

Given the reliability of high-power capacitors holds paramount importance in practical applications, the energy storage performance of sample S2 at different temperatures, frequencies, and cycles of the applied electric field was further investigated. As shown in Fig. S2(a), P - E loop under 350 kV/cm was tested from 25°C to 150°C and temperature-dependent energy storage performance was plotted. It was

observed that the P_{\max} value decreased slightly with increasing temperature, but W_{rec} and η remained consistently high, exceeding 3.1 J/cm^3 and 90%, respectively, with changes of less than 10% and 1%, respectively. This finding underscores the suitability of sample S2 for use at elevated temperatures. In addition, Fig. S2 (b) depicts the P - E loops of the sample S2 at different frequencies (5-500 Hz) and the corresponding energy storage performance under 350 kV/cm. The W_{rec} and η values preserve at high levels of 3.5 - 3.4 J/cm^3 and 91-96%, respectively, suggesting excellent frequency insensitivity properties.

Figure S2 (c) shows the unipolar P - E loops of sample S2 after different cycling numbers under 350 kV/cm, indicating that the P - E loops were able to maintain a slim shape with a high P_{\max} over a cycling range of 10^0 - 10^5 , where the W_{rec} and η were found to show minimal variations. This indicates that the energy storage performance exhibits minimal degradation after undergoing 10^5 charge/discharge cycles, demonstrating excellent fatigue resistance.

Under-damped and over-damped charge/discharge measurements were performed to simulate actual energy storage and discharge performance in high-power pulse devices. The current-time (I - t) curve is shown in Figs.1(e) and (f). The current density (C_D), power discharge density (P_D), discharge time ($t_{0.9}$) and discharge energy density (W_D) were calculated by using the method described in Reference [42]. In addition, sample S2 exhibits a remarkable charge/discharge performance under over-damped test at a fixed load resistance of 300Ω , with a high discharge speed, $t_{0.9}=58 \text{ ns}$, as shown in Fig.1 (f).

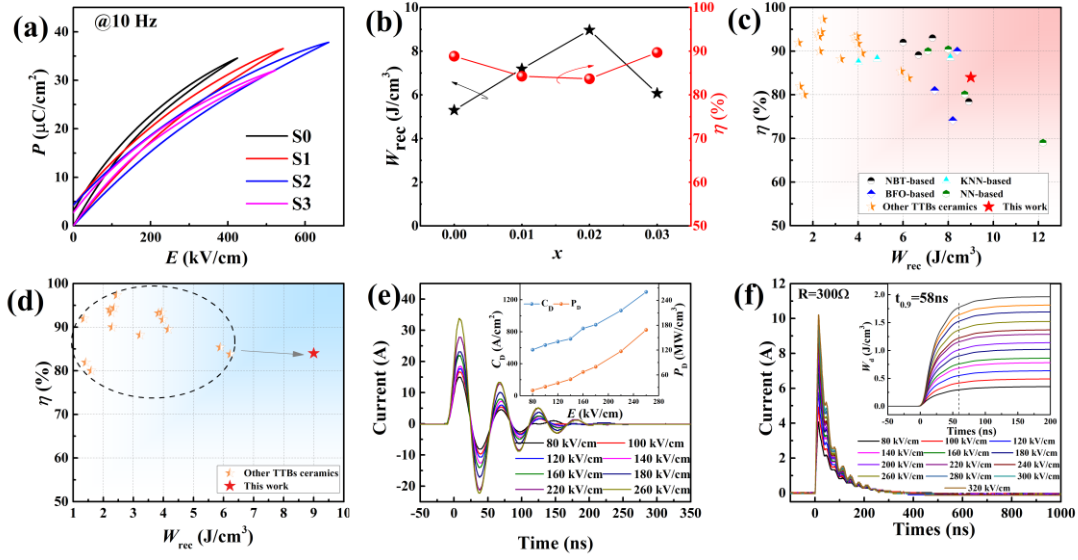


Figure 1. (a) Unipolar P - E loops of all GBSSN samples under a breakdown electric field. (b) calculated W_{rec} and η under E_b from unipolar hysteresis loops. (c) Comparison of the W_{rec} versus η of ceramic S2 with other representative lead-free ceramics reported previously^[17-30] and (d) W_{rec} versus η with other TTBs ceramics reported previously^[6-7, 13-15, 31-41]. (e) Under-damped discharge waveforms of the S2 sample as a function of time, the inset shows the current density (C_D) and power discharge density (P_D) as a function of applied electric fields; (f) Over-damped discharging current (I - t) curves of the S2 sample ceramic in connection with a fixed load resistance of 300 Ω under various electric fields, and the inset shows the discharge energy density (W_D - t) curves.

Figures S3(a)-(d) display SEM images of GBSSN ceramics, and the inset illustrates the statistical grain size distribution of the corresponding sample. As the Sm^{3+} content increases, the average grain size of GBSSN gradually decreases, with S2 presenting the smallest average grain size of 2.2 μm , representing a decrease of 30% compared with that of S0 ($\sim 3.2 \mu\text{m}$). The suppressed grain growth in this context can be attributed to the fact that the higher atomic mass of the doped Sm^{3+} reduces the ionic diffusion rate during the sintering process^[43].

It is generally believed that a decrease in average grain size (G_a) is associated with

an increase in E_b , which follows an exponential decay relationship with grain size (i.e., $E_b \propto (G_a)^{-1}$ [24, 44]). This can be attributed to the fact that the depletion layer in the grain boundary provides a higher barrier for the transfer of ions and electrons^[45]. As the Sm^{3+} doping level increases, non-equiaxed grains evolve into equiaxed grains without any abnormal grains, thereby increasing the density of grain boundaries and consequently enhancing the breakdown strength. In Fig. S3(e), it is evident that the S2 sample displays a uniform element distribution without any sensible segregation, demonstrating that Sm^{3+} has been successfully incorporated into the lattice. This homogeneous composition, along with the refined grain size, is beneficial for boosting the breakdown strength and optimizing the overall energy storage performance^[46].

Figure 2(a) shows that the ceramics with x ranging from 0 to 0.03 present a TTB phase (PDF#39-0265) without any detectable secondary phase. The enlargement of the local region in Fig. 2(a) is displayed in Fig. 2(b). As the amount of Sm^{3+} doping level increases, the peaks of (330) and (311) shift to high angle due to the smaller radius of Sm^{3+} (1.24 Å) compared to that of Ba^{2+} (1.61 Å) and Sr^{2+} (1.44 Å), indicating that doping leads to a decrease in the interplanar spacing and compression of the unit cell volume. In addition, two diffraction peaks near 46° , the low-angle (002) peak and the high-angle (620) peak, gradually merge, which may be associated with a decreased tetragonality^[11]. To gain a better understanding of the effect of Sm^{3+} doping on the crystal structure of GBSN ceramics, Rietveld refinement was conducted on the XRD patterns of samples S0-S3, and the results and crystallographic data are presented in Fig. S4 and Table S1, respectively. These results show that all the samples are in the

p4bm phase, and the c/a ratio gradually decreases, leading to a decrease in electrical polarization and a moderate dielectric constant^[47].

Figure 2(c) displays the Raman spectra of the GBSSN ceramics, which reveals three main regions of interest: (I) the peaks below 200 cm^{-1} , which are attributed to the displacement of A-site ions relative to the NbO_6 octahedra tilt^[48]; (II) the ν_5 mode at around 250 cm^{-1} , which is associated with O-B-O bending vibrations; and (III) the ν_2 mode at around 630 cm^{-1} , which is linked to B-O stretching vibrations^[41]. Fig. 2(d) shows the Raman peak positions and full width at half maximum (FWHM) of the ν_5 and ν_2 modes for different samples, which have been fitted by a Gauss-Lorentz function. It is observed that the smaller ionic radius of Sm^{3+} leads to a redshift in the ν_2 and ν_5 modes, thus increasing the stretching vibration and reducing the interaction between cations and anions. This further promotes the expansion of the BO_6 octahedron^[14], and weakens the B-O covalent bond. Moreover, the increased FWHM of the ν_5 and ν_2 modes is indicative of a higher degree of distortion in the BO_6 octahedron and the enhanced disorder in the short-range structure. Figure 2(e) shows the projection of GBSSN unit cell taking along [001] direction (P4bm, solid line). The substitution of Sr^{2+} by Sm^{3+} will create vacancies in A-site. Therefore, compared with sample S0, the increased A-site vacancy density in sample S2 is accompanied by more non-conserved charges in the local area^[49]. The broken long-range order caused by such defects also results in an increased degree of relaxation^[50].

In order to delve deeper into the origin of the relaxation of GBSSN ceramics, we conducted a thorough examination of the microstructures of both S0 and S2, using field emission transmission electron microscopy. Figure 2(f) shows a transmission electron microscopy (TEM) image with the associated selected area electron diffraction (SAED) pattern of S0 along the [110] zone axis. The SAED pattern reveals the presence of weak satellite reflections, indicative of incommensurate modulations (indicated by the red arrows), in addition to the diffraction corresponding to the TTB phase. Figure 2(g) and Fig. S5(a)-(c) present the SAED patterns of S2 along the [110] zone axis over a temperature range of 100 K to 373 K. Similar to S0, these patterns exhibit subcell reflections associated with incommensurate superlattices alongside the diffraction corresponding to TTBs (indicated by the red arrows) at room temperature. Notably, the subcell diffraction of S2 ceramics vanishes at 373K, implying the disappearance of the incommensurate superlattice.

It is believed that the commensurate modulation is strongly correlated to the displacement of cations, giving rise to the formation of long-range dipole order and a ferroelectric transition. In contrast, the presence of an incommensurate modulation is linked to the onset of a relaxor ferroelectric transition^[51-52]. The incommensurate modulation vector was calculated to be $(1/4+\delta)(\mathbf{a}^*-\mathbf{b}^*)+1/2\mathbf{c}^*$ (where \mathbf{a}^* , \mathbf{b}^* , and \mathbf{c}^* define the distances of the diffraction spots and δ defines a standard divergence from the commensurate modulation that is identified as $\delta = (x-y)/(x+y)$, for which x and y are the distances from the adjacent incommensurate diffraction spots) by measuring the positions of weak reflections^[51]. The schematic diagram for the determination of the

incommensurate superlattice incommensurability parameter δ is shown in Fig. 2(h). The calculation results are: $\delta_{S0}=0.151\pm0.01$ (300K), $\delta_{S2}=0.357\pm0.08$ (100K), $\delta_{S2}=0.303\pm0.06$ (200K) and $\delta_{S2}=0.283\pm0.06$ (300K). An argument has been put forth suggesting that the enhanced disorder of the A-site generates incommensurate diffraction spots ^[52]. Therefore, the larger δ value observed in S2 is attributed to the random occupancy of Ba²⁺ and Sm³⁺ in the A-site and thus introducing a structural disorder that increases the relaxation behavior ^[53]. This relaxation behavior delays the saturation of polarization, enabling the achievement of high P_{\max} under a higher electric field, thus contributing to superior energy storage performance^[54-55].

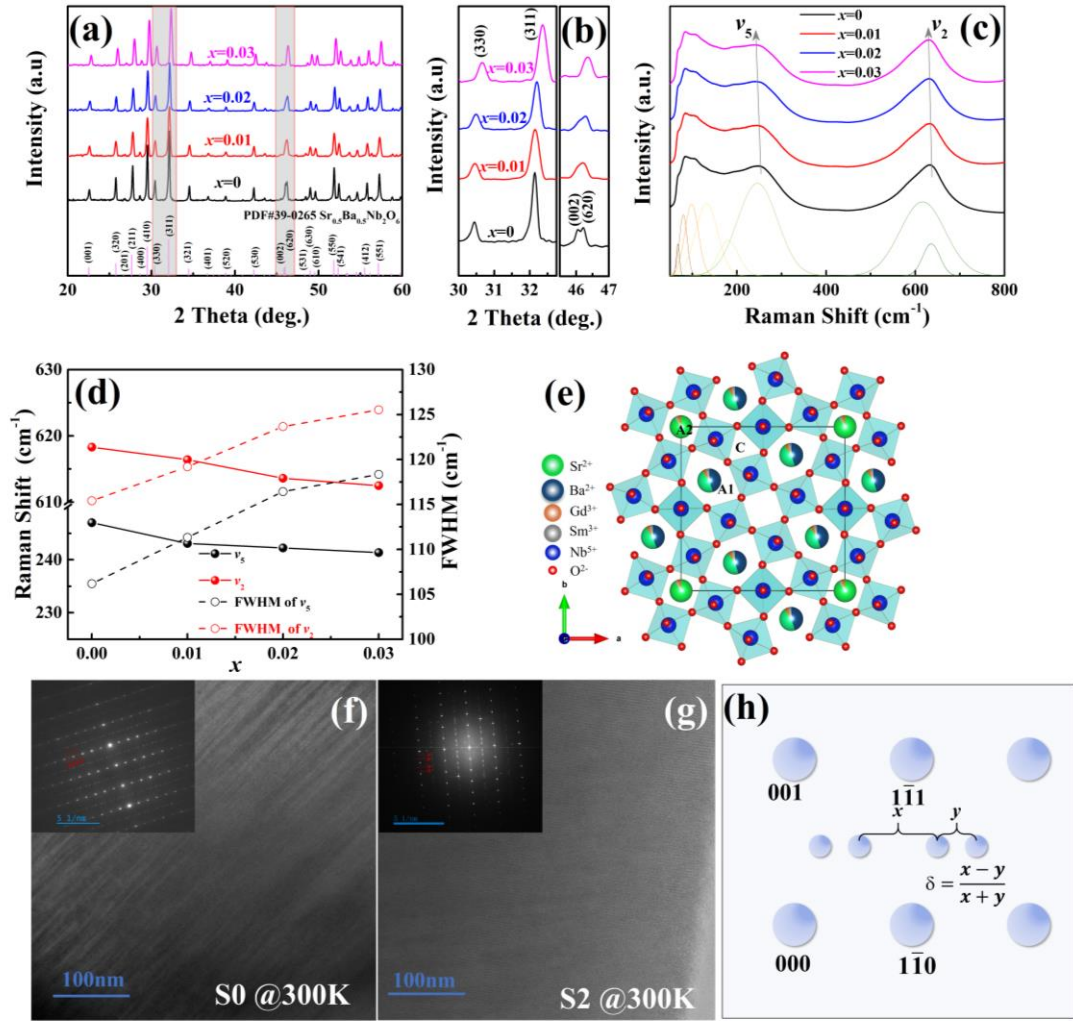


Figure 2. (a) The XRD pattern of the GBSSN samples. (b) Enlarged views of the (330), (311), (002) and (620) peaks. (c) Raman spectra of GBSSN at room temperature and (d) Raman peak positions and the FWHM of ν_5 , ν_2 mode as a function of Sm^{3+} content, derived from fitting the spectra with the Gauss-Lorentz function. (e) Projection of GBSSN unit take along [001] (P4bm, solid line). (f) TEM image and SAED patterns take along [110] zone from S0 samples at 300 K, (g) TEM image and SAED patterns take along [110] zone from S2 samples at 300 K. The red arrows indicate the appearance of the satellite reflections for incommensurate modulation in (f)-(g). (h) The measurement schematic to determine the incommensurate superlattice incommensurability parameter δ ^[51].

To study the evolution of relaxation behavior, the dielectric constant (ϵ_r) and $\tan\delta$ of all GBSSN ceramics across a temperature range of 25~150 °C and frequency range of 10 Hz to 2 MHz were measured, as shown in Figs. S6(a)-(h). It is evident that the

broadened dielectric peaks, together with a conspicuous frequency dispersion behavior, showcase the unique dispersed phase transition, akin to the reported perovskite relaxor ferroelectrics.

To gain a better understanding of the physical origin of the relaxation behavior observed in GBSSN ceramics, the relaxation dynamic behaviors were evaluated by the Vogel-Fulcher model^[56], which can be expressed as:

$$f = f_0 \exp\left(\frac{E_a}{k(T_m - T_f)}\right) \quad (5)$$

where f_0 is an attempt frequency, E_a the activation energy, k the Boltzmann constant, T_m the temperature at the maximum dielectric constant and T_f the freezing temperature.

According to the Vogel-Fulcher law, the corresponding parameters were calculated and the fitting results are shown in Fig. S6. The calculated activation energy for the GBSSN ceramic system is illustrated in Fig. 3(a). It is observed that as the Sm^{3+} doping level increases, the activation energy increases from 0.013 eV to 0.16 eV. Table S2 summarizes the corresponding factors obtained by fitting the Vogel-Fulcher law for various relaxors. It is evident that the E_a of sample S2 surpasses that of the majority of the relaxors detailed in Table S2, especially TTBs ceramics. This enhanced activation energy suggests that the polar clusters (or polar nano regions, PNRs) within the system are discrete and frustrated, resulting in a weaker coupling between the neighboring clusters^[57]. Furthermore, under field-cooled conditions, the formation of long-range dipole arrangements becomes challenging^[58-59], but the application of high fields can

still induce the dipole switching, even at low temperatures. This is beneficial for energy storage, as it is associated with a higher polarization saturation field and a slimmer P - E loop (or lower energy loss) [56]. As shown in the schematic diagram in Fig.3(b), the height of the arc represents the value of the activation energy. Due to the increase in E_a , the potential barrier of interaction between PNRs increases, making it more difficult to reach a consistent orientation and acquire macroscopic polarization. As the coupling strength between PNRs becomes weaker, a higher electric field will necessitate overcoming this potential barrier to obtain a substantial macroscopic polarization[20].

To intuitively visualize the weakly coupled PNRs induced by the Sm^{3+} doping in GSBN ceramics, comprehensive TEM and scanning TEM (STEM) investigations were conducted on S0 and S2 samples, as illustrated in Figs. 3(c)-(e). In the S0 sample (Fig. 3(c)), distinct domain structures or ordered polar regions were clearly observed, with widths extending to several tens of nanometers. In stark contrast, no such domains were visible in the S2 sample (Fig. 3(d)). To explore the presence of local orders at a smaller scale in the S2 sample, atomic-resolution high-angle annular dark-field (HAADF)-STEM images were captured along the $[100]_c$ direction of the S2 sample, as illustrated in Fig. 3(e). The HAADF-STEM images corroborated that, akin to the perovskite structure, the displacement of B-site cations plays a critical role in producing the polarization within the TTB structure[12]. Notably, the B-site Nb cations exhibited substantial displacement, as shown in the bottom right panel of Fig. 3(e). This displacement is expected to impact the local dipole moment, subsequently influencing the local polarization and contributing to the formation of PNRs. By analyzing the

motion of the central Nb cations relative to the neighboring two Nb cations, the local polarization direction was acquired and indicated with yellow arrows. Based on this analysis, regions with approximately identical polarization directions were identified, denoted by dashed ellipses in distinct colors in Fig. 3(e). These short-range dipole ordering regions were measured at scales ranging from two nanometers to several nanometers, confirming the existence of small-scale PNRs in the S2 sample. In comparison to GBSN with long-range dipole ordering and large-scale nanodomain structures, the introduction of Sm^{3+} in GBSN evidently disrupts the coupling between nearby dipoles, thereby inhibiting the formation of large-sized ferroelectric nanodomains and resulting in discrete polar clusters (weakly coupled PNRs) with inconsistent orientations^[60]. The combination of high breakdown strength and the presence of weakly coupled PNRs in the S2 sample results in ultra-high energy storage performance.

Figure S7(a) shows the temperature dependence of the dielectric constant and loss tangent of GBSSN ceramics at 1 kHz. The value of maximum permittivity in GBSSN samples decreases with the increase of Sm^{3+} doping level, while the temperature of maximum dielectric constant (T_m) shifts to a lower temperature. Another characteristic feature of relaxor ferroelectrics is frequency dispersion, where T_m increases as the frequency increases. As depicted in Fig. S7(b), T_m shifts from 307.1 K to 266.4 K (at 10 Hz) and from 336.6 K to 312.1 K (at 2 MHz) with an increase in Sm^{3+} content. Notably, the $\Delta T_m (T_{m\ 2\text{MHz}} - T_{m\ 10\text{Hz}})$ significantly increases from 29.5 K to 45.7 K with the elevation of Sm^{3+} content, indicating the typical diffuse phase transition of GBSSN

relaxor ferroelectrics. In addition, the relaxation characteristics of relaxor can be semi-quantitatively assessed with the diffusion coefficient γ obtained through fitting the modified Curie-Weiss equation^[61]. The fitted values of diffusion coefficient (γ) range from 1.53 to 1.67, as shown in Fig. S7(c), suggesting a strong relaxor behavior of the GBSSN samples.

The dynamic response of GBSSN to applied electric fields was examined utilizing Piezoresponse Force Microscopy (PFM). As shown in Figs. 3(f) and (g), after writing with +10 V and -10 V DC voltage on the top and bottom half of the image, respectively, a read scan was conducted at 4-minute intervals, revealing that polarizations of S2 returned to their initial state (i.e. a highly random state) much more quickly than those in S0. This very fast back switching of polarization suggests the presence of a greater number of dynamic PNRs in S2 ceramics, leading to an increased relaxation behavior. Forming a long range of polarized ordered regions in weakly coupled PNRs poses challenges in the absence of an applied electric field. While they can momentarily align to a consistent polarization direction briefly when subjected to an external electric field, they rapidly revert to their initial state. As shown in Figs. 3 (f4) and (g4), it is evident that after 12 minutes of polarized writing, S2 exhibits virtually no discernible domains compared to S0. This highlights the mutual isolation and weak coupling among polar clusters. The swift reversibility of nanodomains, such as PNRs, results in a smaller remnant polarization, slimmer P - E loops, a relatively high P_{\max} and delayed polarization saturation, all of which are beneficial for a decent energy storage density and efficiency^[59, 62-63].

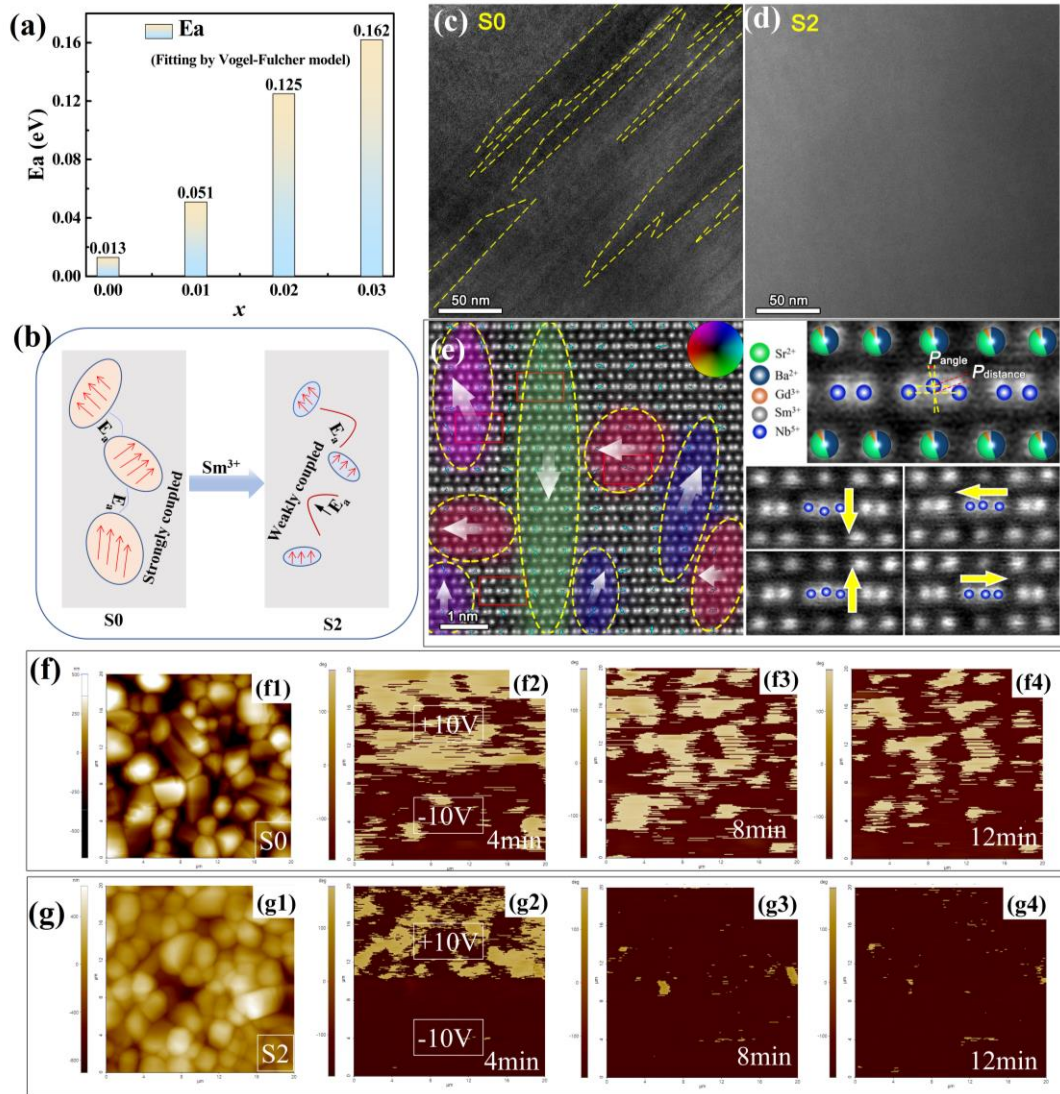


Figure 3. (a) The fitting result of E_a corresponds to the function of Sm^{3+} content by Vogel-Fulcher model. (b) Schematic of PNRs from “strongly coupled” to “weakly coupled” state. (c) and (d) TEM micrographs of S0 and S2 samples, respectively. (e) Atomic-resolution HAADF-STEM image along $[100]_c$ of the S2 sample, and the displacement of B-site cations corresponding to different polarization directions. (g) and (h) Out-of-plane PFM phase images of samples S0 and S2 after poling treatment with ± 10 V and then measuring after a certain relaxation time.

In order to study the evolution of the breakdown field in GBSSN ceramics, impedance measurements were conducted on all samples. The Cole-Cole plots of the electrical impedance of the GBSSN ceramics at temperatures ranging from 450 °C to 675 °C are shown in Fig. S8 (a)-(d). The impedance spectra of S0-S3 at 500 °C, as

shown in Fig. 4(a), reveal that S2 has the largest arc radius, signifying a higher resistivity and consequently a higher breakdown electric field. The resistance of the ceramic is typically attributed to a thermal activation process, as the electrical responses between the grain boundaries and grains differ^[64]. Two sets of equivalent R-C circuit elements were connected in series to fit experimental impedance data for impedance analysis, as shown in the illustration in Fig. 4(a). Two different sets of R-C elements are assigned to represent grains and grain boundaries. The activation energy of conduction (E_a) was calculated using the Arrhenius formula^[65]:

$$R=R_0 \exp(-E_a / kT) \quad (6)$$

where R_0 is a pre-exponential factor, E_a is the activation energy of conduction, k the Boltzmann constant, and T the temperature in Kelvin. The calculated activation energy of conduction for the GBSSN ceramic system is illustrated in Fig. 4(b).

The concept of a higher activation energy value at grain boundary (E_{gb}) has been proposed, corresponding to a lower concentration of free oxygen vacancies at the grain boundaries^[66]. This can be attributed to the presence of a high potential barrier for oxygen vacancies within the grain boundary, which compensates for defects in the grain boundary^[29]. Additionally, it is believed there exists a direct relationship between the activation energy and the breakdown strength^[64]. By introducing Sm^{3+} into the GBSN ceramics, an E_{gb} higher than 1.53 eV can be achieved in S2 samples, which significantly uplifts the breakdown strength.

Figure S9(a) shows the UV-vis absorption spectrum, which demonstrates a shift of absorption edge to a lower wavelength as the doping level increases, indicating an

increase in the band gap. The Tauc plots of GBSSN samples were then made ^[32], as depicted in Fig. 4(c). By fitting the linear section, the band gap values of the corresponding samples were obtained (details of the band gap calculations can be found in the Supporting Information). It was observed that the band gap of the ceramic sample increased from 3.36 eV to 3.47 eV with an increase in the doping level. Dielectric materials with larger bandgaps possess greater intrinsic breakdown strength, as this makes it more difficult for electrons to transit from the valence band to the conduction band ^[67].

To further explore why the S2 sample exhibits a high breakdown field, we conducted tests on the electric-field-induced strain of all GBSSN samples under the same electric field. It is believed that the strain and stress generated by ceramic capacitors under high electric fields can cause the formation of micro-cracks and tensile stress, ultimately leading to the electrical breakdown of ceramics ^[4]. Therefore, to improve the breakdown strength and energy storage density, it is important to reduce the electric-field-induced strain of ceramics ^[68]. As shown in Fig. 4(d), under the same electric field, the electric-field-induced strain of S2 is minimal, reaching 0.013%, which is significantly less than 0.022% of S0. The corresponding *P-E* loops are shown in Fig. S9(b).

The electric field dependence of electric current density and resistivity of all samples were measured at room temperature to illustrate the response of GBSSN ceramics to high DC electric fields more effectively. As demonstrated in Fig. 4(e), the current density of S2 under the same electric field was reduced by about twofold

compared to S0. Additionally, Fig. S9(c) revealed that S2 still had a higher resistivity than S0 under 350 kV/cm, which is in agreement with the impedance results shown above. This demonstrates the critical role of Sm^{3+} doping in achieving a high breakdown strength and energy storage performance. Among the tested samples, S2 showed the smallest electric-field-induced strain, accompanied by its high electrical resistivity and increased bandgap, implying its highest electric breakdown field. The characteristic E_b derived from the standard Weibull distribution^[10] in Fig. 4(f) was evaluated to be 430 kV/cm, 550 kV/cm, 660 kV/cm, and 530 kV/cm for S0-S3, respectively. These values were determined based on the statistical analysis of E_b from testing 10 samples of each composition until breakdown.

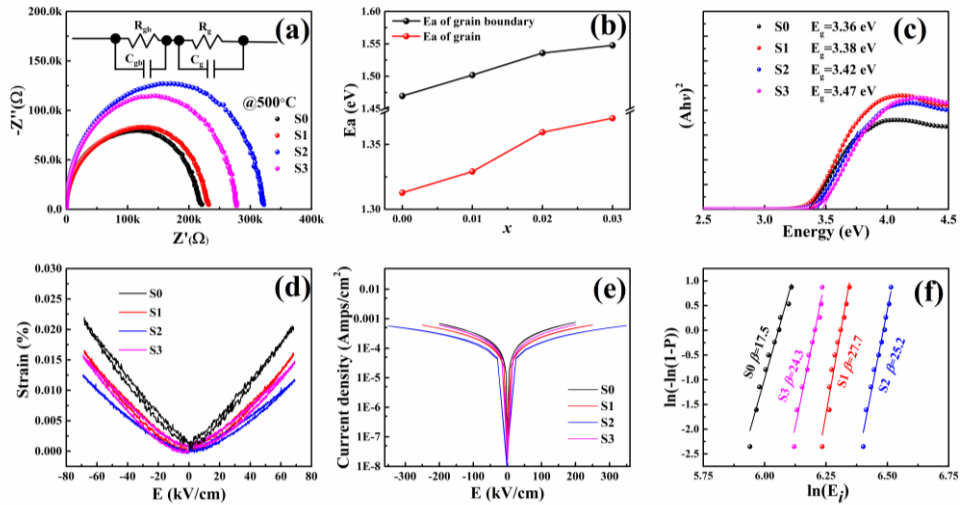


Figure 4. (a) Cole-Cole plots of electrical impedance of S0-S3 at 500 °C. The inset shows the equivalent circuit proposed for impedance data fitting. (b) The fitted grain and grain boundary activation energy values (E_a) versus the Sm^{3+} content. (c) The Tauc plots of all GBSSN samples. (d) Strain versus electric field for GBSSN ceramics. (e) Leakage current density of S0-S3 under different electric fields at room temperature. (f) Weibull distribution of E_b for S0-S3.

3. Conclusions

In this study, a new unfilled TTBs relaxor ferroelectric, prepared through solid-state sintering, has demonstrated exceptional energy storage performance comparable to that of perovskite-structured ceramics. The weakly coupled polar nanodomains in $\text{Gd}_{0.03}\text{Ba}_{0.47}\text{Sr}_{0.455}\text{Sm}_{0.02}\text{Nb}_2\text{O}_6$ (termed S2) yielded an ultrahigh W_{rec} of 9 J/cm^3 and a high efficiency of 84% at room temperature. This remarkable energy storage performance was attributed to the introduction of Sm^{3+} doping, which alters the A-site ion radius and charge disorder, thus disrupting the long-range order of ferroelectrics and creating weakly coupled polar nanoscale domains. Additionally, the refined grain size, increased band gap, reduced electric-field-induced strain and higher activation energy for the conduction of grains and grain boundaries collectively resulted in an ultra-high E_b of 660 kV/cm in the S2 ceramic. Additionally, the energy storage performance of S2 also displayed excellent frequency stability (5-500 Hz), fatigue endurance (up to 10^5 cycles), and temperature stability (25-150°C). Consequently, this study has successfully produced a TTB ceramic with energy storage performance that can rival that of perovskite-structured counterparts, thus opening up possibilities for its application in dielectric ceramic energy storage capacitors.

Experiment procedure

In this work, a series of GBSSN ceramics is prepared by the solid-phase sintering method. The detailed experimental procedures and measuring equipment are illustrated in the Supporting Information.

Acknowledgement

This work was supported by the National Natural Science Foundation of China (NSFC No. 52172125), the National Natural Science Youth Foundation of China (Grant No. 12204393), the Major Science and Technology Project of Ordos City (2021EEDSCXQDFZ014), the Ordos Science and Technology Program (2022YY043), the Basic and Applied Basic Research Major Program of Guangdong Province, China (No. 2021B0301030003), the Project from Xi'an Innovation Design and Research Institute Co., Ltd (20230134), The Shaanxi Province Qin Chuangyuan "Scientists plus Engineers" Team Project (2023KXJ-299), and the Research Grant Council of Hong Kong Special Administrative Region, China (Project No. PolyU25300022).

References

- [1] H. Pan, S. Lan, S. Xu, Q. Zhang, H. Yao, Y. Liu, F. Meng, E.-J. Guo, L. Gu, D. Yi, X. Renshaw Wang, H. Huang, J. L. MacManus-Driscoll, L.-Q. Chen, K.-J. Jin, C.-W. Nan, Y.-H. Lin, *Science* **2021**, *374*, 100.
- [2] B. Yang, Y. Zhang, H. Pan, W. Si, Q. Zhang, Z. Shen, Y. Yu, S. Lan, F. Meng, Y. Liu, H. Huang, J. He, L. Gu, S. Zhang, L.-Q. Chen, J. Zhu, C.-W. Nan, Y.-H. Lin, *Nat. Mater.* **2022**, *21*, 1074.
- [3] H. Qi, A. Xie, A. Tian, R. Zuo, *Adv. Energy Mater.* **2020**, *10*, 1903338.
- [4] L. T. Yang, X. Kong, F. Li, H. Hao, Z. X. Cheng, H. X. Liu, J. F. Li, S. J. Zhang, *Prog. Mater. Sci.* **2019**, *102*, 72.
- [5] G. Wang, Z. Lu, Y. Li, L. Li, H. Ji, A. Feteira, D. Zhou, D. Wang, S. Zhang, I. M. Reaney, *Chem. Rev.* **2021**, *121*, 6124.
- [6] S. Xu, S. shen, R. Hao, Z. Peng, F. Zhang, D. Wu, P. Liang, X. Chao, L. Wei, Z. Yang, *Chem. Eng. J.* **2022**, *433*, 133812.
- [7] L. Cao, Y. Yuan, Z. Yang, E. Li, S. Zhang, *Ceram. Int.* **2020**, *46*, 6108.
- [8] L. Zhao, Q. Liu, J. Gao, S. Zhang, J.-F. Li, *Adv. Mater.* **2017**, *29*, 1701824.
- [9] J. Kim, S. Saremi, M. Acharya, G. Velarde, E. Parsonnet, P. Donahue, A. Qualls, D. Garcia, L. W. Martin, *Science* **2020**, *369*, 81.
- [10] A. R. Jayakrishnan, J. P. B. Silva, K. Kamakshi, D. Dastan, V. Annapureddy, M. Pereira, K. C. Sekhar, *Prog. Mater. Sci.* **2023**, *132*, 101046.
- [11] M. C. Stennett, I. M. Reaney, G. C. Miles, D. I. Woodward, A. R. West, C. A. Kirk, I. Levin, *J. Appl. Phys.* **2007**, *101*.
- [12] V. V. Shvartsman, D. C. Lupascu, *J. Am. Ceram. Soc.* **2012**, *95*, 1.
- [13] L. Cao, Y. Yuan, X. Meng, E. Li, B. Tang, *ACS Appl. Mater. Interfaces* **2022**, *14*, 9318.
- [14] H. Peng, Z. Liu, Z. Fu, K. Dai, Z. Lv, S. Guo, Z. Hu, F. Xu, G. Wang, *Adv. Sci* **2023**, *10*, 2300227.
- [15] B. Yang, Y. Gao, X. Lou, Y. Yang, Y. Hu, G. Zhang, S. Sun, *Energy Stor. Mater.* **2023**, *55*, 763.
- [16] D. Li, D. Zhou, D. Wang, W. Zhao, Y. Guo, Z. Shi, T. Zhou, S.-K. Sun, C. Singh, S. Trukhanov, A. S. B. Sombra, *Small* **2023**, *19*, 2206958.
- [17] M. Zhang, H. Yang, Y. Lin, Q. Yuan, H. Du, *Energy Stor. Mater.* **2022**, *45*, 861.

-
- [18] Y. Zhang, R. Zuo, *J. Eur. Ceram. Soc.* **2020**, *40*, 5466.
- [19] F. Yan, H. Bai, G. Ge, J. Lin, C. Shi, K. Zhu, B. Shen, J. Zhai, S. Zhang, *Small* **2022**, *18*, 2106515.
- [20] J. Zhao, T. Hu, Z. Fu, Z. Pan, L. Tang, X. Chen, H. Li, J. Hu, L. Lv, Z. Zhou, J. Liu, P. Li, J. Zhai, *Small* **2023**, *19*, 2206840.
- [21] Z. Lu, G. Wang, W. Bao, J. Li, L. Li, A. Mostaed, H. Yang, H. Ji, D. Li, A. Feteira, F. Xu, D. C. Sinclair, D. Wang, S.-Y. Liu, I. M. Reaney, *Energy & Environmental Science* **2020**, *13*, 2938.
- [22] S. Wu, B. Fu, J. Zhang, H. Du, Q. Zong, J. Wang, Z. Pan, W. Bai, P. Zheng, *Small* **2023**, *n/a*, 2303915.
- [23] R. Kang, Z. Wang, M. Wu, S. Cheng, S. Mi, Y. Hu, L. Zhang, D. Wang, X. Lou, *Nano Energy* **2023**, *112*, 108477.
- [24] Y. Gao, X. Zhu, B. Yang, P. Shi, R. Kang, Y. Yuan, Q. Liu, M. Wu, J. Gao, X. Lou, *Chem. Eng. J.* **2021**, 133584.
- [25] A. Xie, R. Zuo, Z. Qiao, Z. Fu, T. Hu, L. Fei, *Adv. Energy Mater.* **2021**, *11*, 2101378.
- [26] L. Liu, Y. Liu, J. Hao, J. Chen, P. Li, S. Chen, P. Fu, W. Li, J. Zhai, *Nano Energy* **2023**, *109*, 108275.
- [27] W. Cao, P. Chen, R. Lin, F. Li, B. Ge, D. Song, Z. Cheng, C. Wang, *Compos. B. Eng.* **2023**, *255*, 110630.
- [28] X. Wang, Y. Huan, P. Zhao, X. Liu, T. Wei, Q. Zhang, X. Wang, *J. Materiomics* **2021**, *7*, 780.
- [29] H. Chen, J. Shi, X. Chen, C. Sun, F. Pang, X. Dong, H. Zhang, H. Zhou, *J. Mater. Chem. A* **2021**, *9*, 4789.
- [30] H. Qi, R. Zuo, A. Xie, A. Tian, J. Fu, Y. Zhang, S. Zhang, *Adv. Funct. Mater.* **2019**, *29*, 1903877.
- [31] H. Wang, X. Bu, X. Zhang, P. Zheng, L. Li, F. Wen, W. Bai, J. Zhang, L. Zheng, Y. Zhang, *ACS Appl. Energy Mater.* **2021**, *4*, 9066.
- [32] L. Cao, Y. Yuan, E. Li, S. Zhang, *Chem. Eng. J.* **2021**, *421*, 127846.
- [33] X. Zhang, H. Wang, X. Bu, P. Zheng, L. Li, F. Wen, W. Bai, J. Zhang, L. Zheng, J. Zhai, Y. Zhang, *Inorg. Chem.* **2021**, *60*, 6559.
- [34] C. Luo, C. Zhu, Y. Liang, P. Zheng, W. Bai, L. Li, F. Wen, J. Zhang, L. Zheng, Y. Zhang, *ACS Appl. Electron. Mater* **2022**, *4*, 452.
- [35] L. Cao, Y. Yuan, B. Tang, E. Li, S. Zhang, *J. Eur. Ceram. Soc.* **2020**, *40*, 2366.
- [36] X. Zhang, P. Zheng, L. Li, F. Wen, W. Bai, J. Zhang, L. Zheng, Y. Zhang, *Scr. Mater.* **2022**, *211*, 114514.
- [37] H. Bai, J. Li, Y. Wu, Y. Hong, K. Shi, Z. Zhou, *Ceram. Int.* **2019**, *45*, 11109.
- [38] C. Luo, X. Zheng, P. Zheng, J. Du, Z. Niu, K. Zhang, W. Bai, Q. Fan, L. Zheng, Y. Zhang, *J. Alloys Compd.* **2023**, *933*, 167809.
- [39] X. Zhang, W. Ye, X. Bu, P. Zheng, L. Li, F. Wen, W. Bai, L. Zheng, Y. Zhang, *Dalton Trans.* **2021**, *50*, 124.
- [40] S. Xu, S. Shen, C. Huang, Y. He, X. Chao, D. Wu, P. Liang, Z. Yang, J. Lu, L. Wei, *ACS Appl. Mater. Interfaces* **2023**.

-
- [41] S. Hou, S. Xu, L. Yang, X. Liu, L. Wei, X. Chao, D. Wu, P. Liang, Z. Yang, *Ceram. Int.* **2022**, *48*, 28382.
- [42] Z. Pan, D. Hu, Y. Zhang, J. Liu, B. Shen, J. Zhai, *J. Mater. Chem. C* **2019**, *7*, 4072.
- [43] L. Zhang, X. Y. Pu, M. Chen, S. S. Bai, Y. P. Pu, *J. Eur. Ceram. Soc.* **2018**, *38*, 2304.
- [44] T. Tunkasiri, G. Rujijanagul, *J. Mater. Sci. Lett.* **1996**, *15*, 1767.
- [45] R. Waser, *Ferroelectrics* **1992**, *133*, 109.
- [46] Z. Yao, Z. Song, H. Hao, Z. Yu, M. Cao, S. Zhang, M. T. Lanagan, H. Liu, *Adv. Mater.* **2017**, *29*, 1601727.
- [47] J. Gardner, F. D. Morrison, *Dalton Trans.* **2014**, *43*, 11687.
- [48] B. Yang, S. Hao, P. Yang, L. Wei, Z. Yang, *Ceram. Int.* **2018**, *44*, 8832.
- [49] W.-B. Li, D. Zhou, L.-X. Pang, *Appl. Phys. Lett.* **2017**, *110*, 132902.
- [50] X. Zhao, W. Bai, Y. Ding, L. Wang, S. Wu, P. Zheng, P. Li, J. Zhai, *J. Eur. Ceram. Soc.* **2020**, *40*, 4475.
- [51] L. A. Bursill, P. J. Lin, *Acta Cryst. B* **1987**, *43*, 49.
- [52] I. Levin, M. C. Stennett, G. C. Miles, D. I. Woodward, A. R. West, I. M. Reaney, *Appl. Phys. Lett.* **2006**, *89*, 122908.
- [53] X. L. Zhu, K. Li, X. M. Chen, *J. Am. Ceram. Soc.* **2014**, *97*, 329.
- [54] X. Zhu, Y. Gao, P. Shi, R. Kang, F. Kang, W. Qiao, J. Zhao, Z. Wang, Y. Yuan, X. Lou, *Nano Energy* **2022**, *98*, 107276.
- [55] L. Yang, X. Kong, Z. Cheng, S. Zhang, *J. Mater. Chem. A* **2019**, *7*, 8573.
- [56] S. Nayak, S. Venkateswarlu, A. S. Budisuharto, M. R. V. Jørgensen, O. Borkiewicz, K. A. Beyer, A. Pramanick, *J. Am. Ceram. Soc.* **2019**, *102*, 5919.
- [57] K. Chen, Q. Zhang, J. Liu, J. Wang, Z. Lan, L. Fang, C. Hu, N. Luo, B. Peng, C. Long, D. Wang, L. Liu, *physica status solidi (a)* **2022**, *219*, 2100579.
- [58] H. Ogihara, C. A. Randall, S. Trolier-McKinstry, *J. Am. Ceram. Soc.* **2009**, *92*, 110.
- [59] H. Pan, J. Ma, J. Ma, Q. Zhang, X. Liu, B. Guan, L. Gu, X. Zhang, Y.-J. Zhang, L. Li, Y. Shen, Y.-H. Lin, C.-W. Nan, *Nat. Commun.* **2018**, *9*, 1813.
- [60] A. Pramanick, S. Nayak, T. Egami, W. Dmowski, A. S. Budisuharto, F. Marlton, M. R. V. Jørgensen, S. Venkateswarlu, K. A. Beyer, *Physical Review B* **2021**, *103*, 214105.
- [61] Y. Zhi, A. Chen, P. M. Vilarinho, P. Q. Mantas, J. L. Baptista, *J. Eur. Ceram. Soc.* **1998**, *18*, 1613.
- [62] R. Dittmer, W. Jo, J. Rödel, S. Kalinin, N. Balke, *Adv. Funct. Mater.* **2012**, *22*, 4208.
- [63] Y. Lin, D. Li, M. Zhang, S. Zhan, Y. Yang, H. Yang, Q. Yuan, *ACS Appl. Mater. Interfaces* **2019**, *11*, 36824.
- [64] L. Zhang, Y. Pu, M. Chen, *Mater. Today Chem.* **2023**, *28*, 101353.
- [65] J. T. S. Irvine, D. C. Sinclair, A. R. West, *Adv. Mater.* **1990**, *2*, 132.
- [66] Y. Sun, H. Liu, H. Hao, S. Zhang, *J. Am. Ceram. Soc.* **2016**, *99*, 3067.
- [67] C. Kim, G. Pilania, R. Ramprasad, *J. Phys. Chem. C* **2016**, *120*, 14575.

[68] J. Li, Z. Shen, X. Chen, S. Yang, W. Zhou, M. Wang, L. Wang, Q. Kou, Y. Liu, Q. Li, Z. Xu, Y. Chang, S. Zhang, F. Li, *Nat. Mater.* **2020**, *19*, 999.